Chemical Science

ROYAL SOCIETY OF CHEMISTRY

EDGE ARTICLE

View Article Online
View Journal

Cite this: DOI: 10.1039/d6sc01740a

All publication charges for this article have been paid for by the Royal Society of Chemistry

Data-driven structural angle mining elucidates hidden design rules for hydrogen evolution single-atom electrocatalysts

Bingqing Ge,†[acd] Yang Chen,†[b] Yidi Wu,†[ac] Fenfei Wei,[cd] Fengyu Li,[f] Lulu Chen,[ac] Jian Lin,*[b] Xianzhi Fu[ac] and Sen Lin*[ace]

Structural distortions in modified two-dimensional transition metal dichalcogenides (MX_2) influence electrocatalytic activity, yet quantitative and predictive structure–property relationships remain underdeveloped. To bridge this gap, we perform data-driven structural angle mining across hundreds of thousands of single-atom doped configurations ($TM_1@MX_2$) and establish geometrically defined angular descriptors. These descriptors exhibit high predictive accuracy for hydrogen evolution electrocatalysis. Crucially, our analysis reveals that catalytic activity correlates more strongly with long-range angular parameters describing peripheral geometric effects than with the local coordination environment. Guided by these descriptors, we identify specific angular signatures as quantitative predictors for high-performance catalysts: an outer-shell S-centered angle indicates optimal hydrogen evolution reaction (HER) activity for $Ir_1@MoS_2$ (S-vacancy), while a distinct Mo-centered angle identifies $V_1@MoS_2$ (Mo-vacancy) as a promising earth-abundant candidate. Experimental verification confirms these predictions: synthesized $Ir_1@MoS_2$, with an ultralow loading of 0.1 wt%, achieves performance comparable to commercial Pt/C on a mass-activity basis, while $V_1@MoS_2$ enhances HER performance relative to pristine MoS_2. The framework also shows strong computational correlations with oxygen evolution activity, though experimental validation for OER remains an important direction for future investigation. The angular descriptor framework introduced here provides a geometrically intuitive and electronically grounded strategy for the rational design and accelerated discovery of advanced energy materials.

Received 1st March 2026
Accepted 1st June 2026

DOI: 10.1039/d6sc01740a

rsc.li/chemical-science

Introduction

The transition to a sustainable energy future is contingent on the development of efficient electrocatalysts for water splitting, a key technology for green hydrogen production. However, widespread deployment of electrolyzers remains constrained by their reliance on scarce platinum-group metals, spurring the search for earth-abundant alternatives without compromising activity.[1–4] While single-atom catalysts (SACs) embedded in two-dimensional transition metal dichalcogenides ($TM_1@MX_2$) present a promising platform to reduce reliance on platinum-group metals, their rational design remains fundamentally challenging.[5–8] The catalytic performance is exquisitely sensitive to the local atomic environment, where subtle structural distortions can dramatically modulate activity.[9–14] However, a critical gap persists between observing these structural effects and quantitatively predicting them, as current paradigms struggle to decouple the intricate interplay between geometry and electronic structure.

The descriptor-based approach, central to modern catalyst design, has long been dominated by electronic structure parameters, such as adsorption energies and d-band centers.[15–20] While powerful, these descriptors often serve as computational proxies that are notoriously difficult to translate into actionable synthesis guidelines. There exists a critical gap between the abstract electronic parameters and the tangible geometric structures that chemists manipulate. They answer the "what" but not the "how", failing to provide experimentalists with clear geometric blueprints for catalyst creation. Structural descriptors present a compelling alternative,[21–23] with concepts such as "surface distortion" successfully bridging structure–activity relationships across nanocatalysts.[24]

[a]State Key Laboratory of Chemistry for NBC Hazards Protection, College of Chemistry, Fuzhou University, Fuzhou 350116, China. E-mail: slin@fzu.edu.cn

[b]CAS Key Laboratory of Science and Technology on Applied Catalysis, Dalian Institute of Chemical Physics, Chinese Academy of Sciences, Dalian 116023, China. E-mail: jianlin@dicp.ac.cn

[c]State Key Laboratory of Photocatalysis on Energy and Environment, College of Chemistry, Fuzhou University, Fuzhou 350002, China

[d]Key Laboratory of Mesoscopic Chemistry, School of Chemistry, Nanjing University, Nanjing 210023, Jiangsu, China

[e]College of Chemistry and Chemical Engineering, Institute for Green Chemistry and Environmental Science, Inner Mongolia University, Hohhot, 010021, China

[f]Research Center for Quantum Physics and Technologies, School of Physical Science and Technology, Inner Mongolia University, Hohhot, 010021, China

† These authors contributed equally to this work.

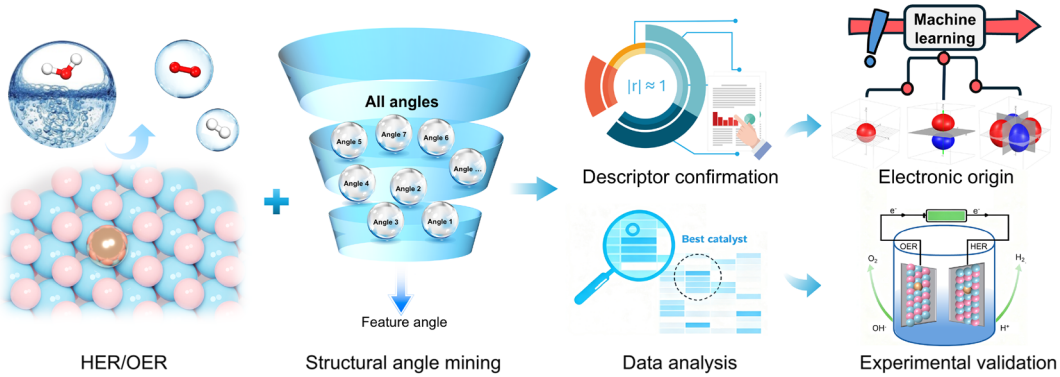

Scheme 1 Integrated workflow from data-driven angular descriptor mining to experimental validation of high-performance water splitting electrocatalyst.

However, such ensemble-averaged structural probes, while insightful, lack the atomic-scale resolution to pinpoint the specific geometric motifs that govern function. This gap between macroscopic observation and atomic-scale design underscores the critical lack of an intuitive, quantitative language to link synthesis to performance.

Efforts to establish such a language by directly linking three-dimensional atomic structure to activity face significant challenges. Pioneering work has highlighted the role of local geometry, using parameters like bond lengths.[25] Despite their utility, such one-dimensional metrics are inherently limited in capturing the multidimensional nature of structural distortion.[26–28] Similarly, coordination numbers often over-simplify the complex, anisotropic coordination environment, failing to resolve critical features beyond the first shell.[29–33] Thus, the pressing need is for multidimensional geometric descriptors that are synthetically interpretable yet rich enough to encode the complexity of atomic-scale environments and to predict their catalytic function.

Here, we introduce data-driven angular descriptors to meet this pressing need. Unlike conventional approaches, these geometric parameters serve as a direct quantitative bridge between the synthesis-induced lattice strain and the resulting catalytic function. We demonstrate that catalytic activity is governed not merely by the local dopant identity, but by the precise angular distortions in the coordination shells. As outlined in Scheme 1, our integrated workflow progresses from data-driven descriptor mining to experimental validation. Through high-throughput density functional theory (DFT) screening of hundreds of thousands of $TM_1@MX_2$ configurations, we establish that catalytic activity is governed not by the local coordination, but by long-range peripheral angles, geometric parameters that are both highly predictive and synthetically interpretable. Crucially, we decode how macroscopic lattice strain manifests in these specific angular motifs, a relationship that shows good transferability across reactions (hydrogen evolution reaction, HER, and oxygen evolution reaction, OER) and materials. Guided by this principle, we discover and experimentally validate two high-performance catalysts: an ultralow-loading $Ir_1@MoS_2$ competitive with Pt/C and an earth-abundant $V_1@MoS_2$. Thereby, we establish angular descriptors as a transformative tool, providing a quantitative, geometry-driven blueprint for rational catalyst design.

Results

Structural angular features

Guided by established experimental frameworks,[34,35] and motivated by the well-recognized catalytic activity of MoS_2 for water electrolysis,[36–39] we systematically investigate two distinct classes of $TM_1@MX_2$ systems classified by vacancy type: chalcogen-vacancy ($TM_1@MX_2$–X) and metal-vacancy ($TM_1@MX_2$–M). Our study encompasses 22 transition metal dopants spanning the 3d, 4d, and 5d series (Fig. 1a), providing broad chemical space exploration while excluding Tc and Hg for safety considerations and Cu, Ag, and Au due to their known catalytic inertness.[40–42] In $TM_1@MX_2$–X systems, each dopant atom occupies an S/Se vacancy site, forming three-fold coordination with three adjacent metal atoms (Fig. 1b and S1). Conversely, for $TM_1@MX_2$–M, each dopant atom occupies an Mo/W vacancy site and adopts six-fold coordination with surrounding chalcogen atoms (Fig. 1c and S2).

The critical role of structural distortions in modulating catalytic performance is well recognized, and dopant-induced lattice distortions are known to perturb electronic structure and influence activity.[43,44] While structural distortion descriptors are gaining attention for accelerating structure–performance understanding,[24,45] more intuitive geometric parameters are still needed. Given that all macroscopic properties originate from atomic arrangements, we identify angular distortions as particularly sensitive metrics for quantifying structure–activity relationships.

Our analysis reveals three fundamental angular distortion modes that define the structural landscape (Fig. 1d): surface distortion, characterizing top-layer geometry; vertical distortion, capturing interlayer interactions; and internal distortion, describing core structural perturbations. Doping-induced variations generate over 190 000 angular configurations per catalyst model, enabling thorough quantification of local geometry.

The microstructure of metal-doped catalysts exhibits well-defined shell environments (Fig. 1e). In $TM_1@MX_2$–X systems, the active site resides at the doped transition metal center, where ligand atoms form concentric shell environments,

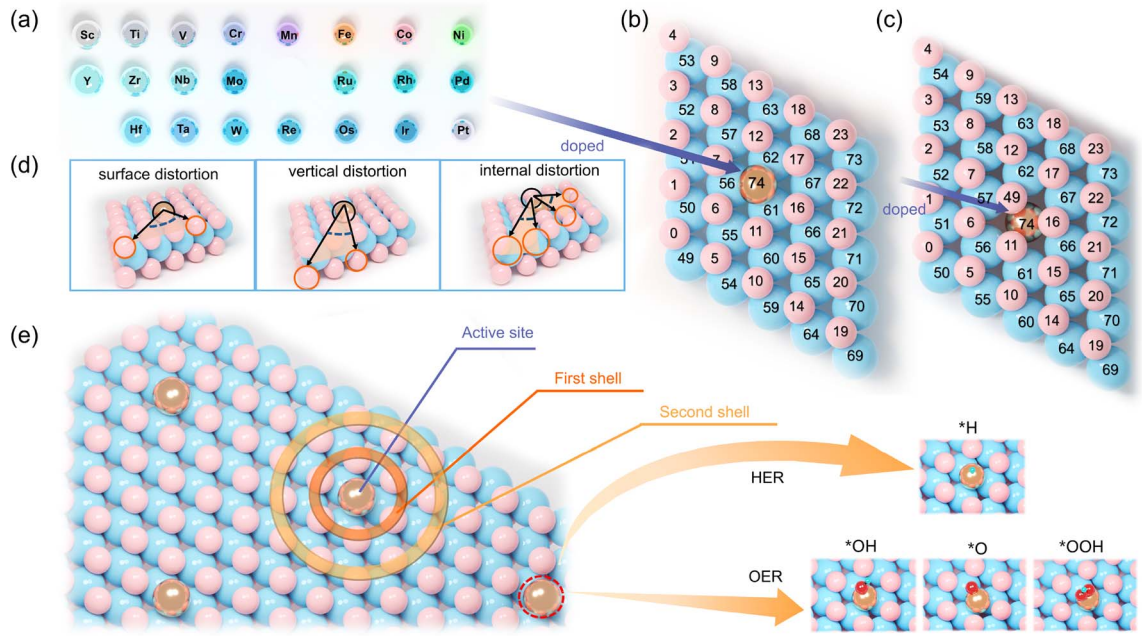

Fig. 1 (a) Periodic table highlighting the 22 transition metal dopants (3d/4d/5d) investigated in this study. (b) Atomic labeling scheme for $TM_1@MX_2$–X: top-layer chalcogens (S/Se, atoms 0–23), bottom-layer chalcogens (24–48), host metal atoms (M = Mo/W, 49–73), and dopant transition metal (TM, atom 74). (c) Atomic labeling for $TM_1@MX_2$–M: top-layer chalcogens (0–23, 49), bottom-layer chalcogens (24–48), host metals (50–73), and dopant (74). (d) Three characteristic distortion modes: surface distortion (angle between vertex and top S/Se atom), vertical distortion (angle between vertex and interlayer S/Se axis), and internal distortion (angle between central Mo/W atom and vertex). (e) Active site geometry in $TM_1@MX_2$–X, showing the doped TM center coordinating key reaction intermediates (*H, *O, *OH, *OOH) for HER/OER processes. The corresponding HER active site configuration for $TM_1@MX_2$–M is provided in Fig. S3. Color scheme: blue = Mo/W atoms, pink = S/Se atoms, gold = dopant atoms.

including the first shell, the second shell, and peripheral shells that coordinate key intermediates (*H, *O, *OH, *OOH) during HER and OER. Different metal dopants induce characteristic distortions across these shell structures, ultimately governing catalytic performance. A similar shell distortion mechanism operates in $TM_1@MX_2$–M systems, though the active center shifts to adjacent chalcogen sites (Fig. S3).

Data-driven development of angular descriptor for HER

To establish quantitative structure–activity relationships for HER, we initially focus on $TM_1@MoS_2$–X as a model system. We start by systematically extracting all structural angles centered at the dopant metal site, defined as the angle formed by the dopant and any two adjacent atoms, which yielded 2631 unique angular parameters. These geometric parameters are rigorously correlated with hydrogen adsorption Gibbs free energy (ΔG_{*H}) using Pearson correlation analysis, with color mapping indicating correlation strength (dark red: strong positive, $r \approx +1$; dark blue: strong negative, $r \approx -1$). Among these, the $\angle S_{17}M_{74}S_{22}$ angle exhibits the strongest correlation ($r = 0.75$, Fig. 2a, S4a and b), suggesting its potential as a HER activity descriptor. However, the moderate correlation coefficient also reveals a fundamental limitation: dopant-centered angles, being spatially localized, fail to fully capture the longer-range structural perturbations that significantly influence catalytic behavior. This finding motivates us to explore the role of extended coordination environments.

The influence of peripheral atomic arrangements on single-atom catalysts has been proposed to arise from microstress variations that propagate across multiple coordination shells.[29–31] Indeed, metal doping not only modifies the electronic structure of the central active site but also induces long-range microstress fields that critically affect HER activity.[46,47] To quantitatively test this hypothesis and develop more accurate structural descriptors, we extend our angle-based analysis to atoms residing in outer coordination shells surrounding the TM_1 centers.

To intuitively visualize the coordination environment, sulfur atoms in equivalent positions are assigned identical colors, with gradation in shading representing increasing shell distance from the active center (Fig. 2a–d). Our systematic analysis reveals a significant trend: the correlation with ΔG_{*H} strengthens as we move from the dopant center toward peripheral atomic shells. The internal angle $\angle S_{23}S_{12}S_{42}$ exhibits a substantially improved correlation ($r = 0.82$; Fig. 2b, S5a and b), compared to dopant-centered descriptors. The trend becomes even more pronounced in the second shell, where surface angle $\angle S_1S_{23}S_8$ shows an even stronger correlation ($r = 0.85$; Fig. 2c, S6a and b), underscoring the critical role of peripheral effects in modulating catalytic performance.

To determine whether this phenomenon extends beyond sulfur-centered coordination, we expand our analysis to angles centered on molybdenum atoms in outer shells. By applying crystallographic symmetry principles, we systematically map Mo coordination environments (Fig. 2d, S7a and b) while

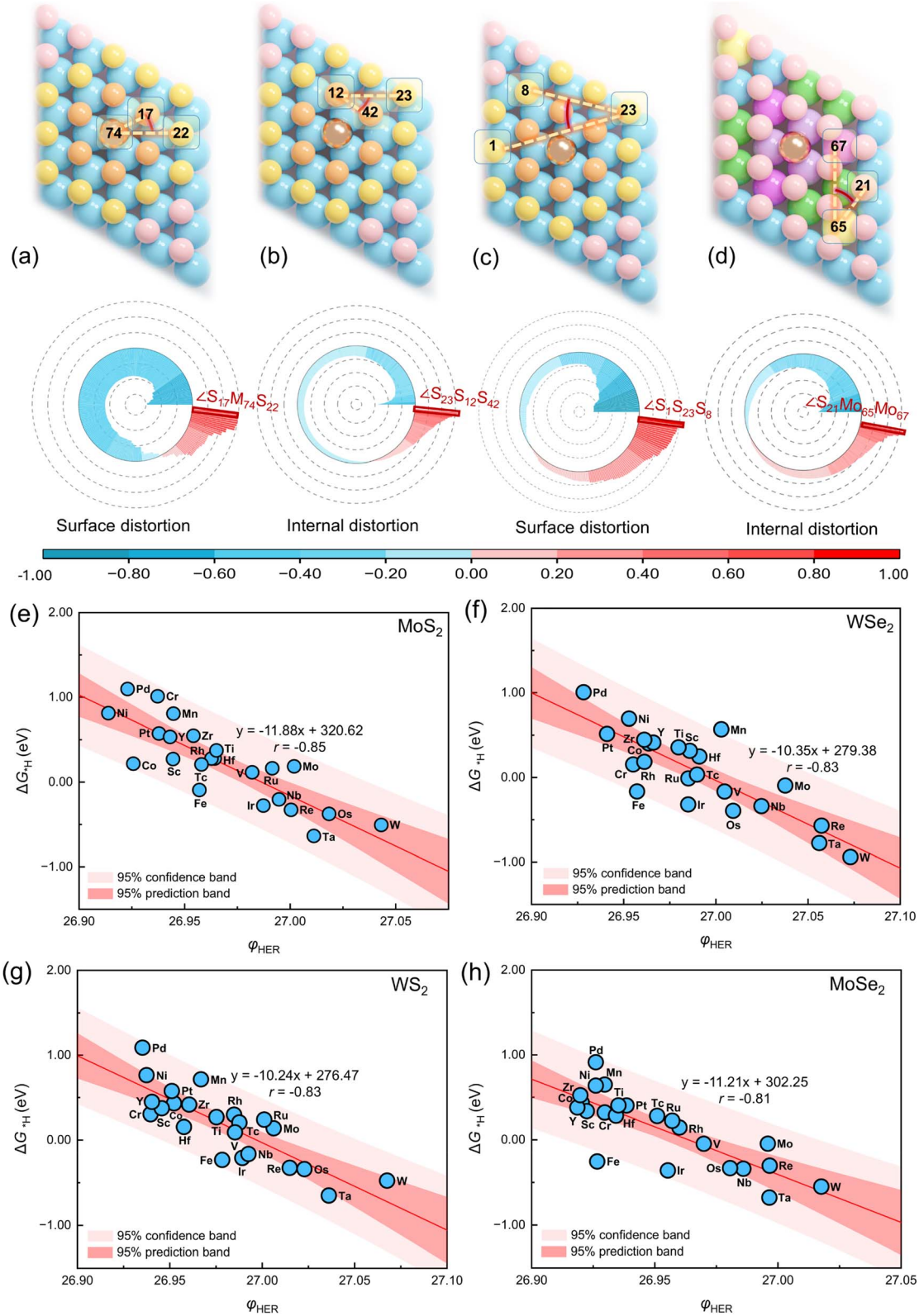

Fig. 2 Correlation analysis of structural distortions with HER activity in TM_1@MoS_2–X. (a–d) Pearson correlation coefficient (r) between ΔG_{*H} and angles centered on (a) dopant atoms, (b) first-shell S atoms, (c) second-shell S atoms, and (d) Mo atoms. The angle exhibiting the strongest linear correlation is highlighted in each panel. (e–h) Linear relationship between the optimal descriptor φ_{HER} and ΔG_{*H} across different substrates: (e) MoS_2, (f) WSe_2, (g) WS_2, and (h) $MoSe_2$. Color scheme: (a–c) structural representations showing the doped transition metal center with first-shell S atoms in orange and second-shell S atoms in yellow. (d) Structural representation showing the doped metal center with first-shell Mo atoms in light purple, second-shell Mo in dark purple, third-shell Mo in green, and outermost-shell Mo in yellow.

maintaining consistent color-coding. Among these, the Mo-centered internal angle $\angle S_{21}Mo_{65}Mo_{67}$ also demonstrates a strong correlation with HER activity ($r = 0.84$, Fig. 2d). Through a comprehensive comparison of all candidate descriptors, we identify the second-shell surface angle $\angle S_1S_{23}S_8$, which exhibits the strongest overall correlation, as the optimal angular descriptor for HER, designated φ_{HER} (Fig. 2e). The consistent superiority of peripheral-shell-centered angles over dopant-site-centered descriptors confirms that long-range structural effects, rather than local metal-centered geometry, predominantly govern HER performance in these SACs.

We further evaluate the transferability of φ_{HER} across different chalcogen-vacancy systems. Impressively, this descriptor maintains strong linear correlations with ΔG_{*H} in $TM_1@WS_2$–S ($r = -0.83$), $TM_1@WSe_2$–Se ($r = -0.83$), and $TM_1@MoSe_2$–Se ($r = -0.81$) (Fig. 2f–h). Within the $TM_1@MoS_2$–S system, $Ir_1@MoS_2$–S emerges as the optimal catalyst, with $\varphi_{HER} = 26.99°$ corresponding to a near-ideal ΔG_{*H} of −0.01 eV (Fig. 2e). Similarly, $Hf_1@WSe_2$–Se, $Ru_1@WS_2$–S, and $Rh_1@MoSe_2$–Se show superior HER activity in their respective systems, with φ_{HER} values of 26.99°, 27.00°, and 26.96°, predicting ΔG_{*H} values of 0.06, −0.04, and 0.41 eV, respectively. This consistent predictive accuracy across diverse material systems establishes φ_{HER} as a robust and generalizable descriptor for structure–activity relationships. These results collectively reveal the intrinsic mechanism of "periphery over core": HER activity is more strongly correlated with the geometric distortion of the peripheral coordination shell than with the locally doped center. Additionally, they validate the good transferability of this type of angular descriptor across different MX_2 hosts. This indicates that the doped atom acts merely as a trigger, while the long-range structural response of the host lattice—quantified by specific peripheral angular configurations—is the key determinant of catalytic performance.

Transferability of angular descriptors from HER to OER

We then aim to determine whether this angular descriptor approach could be extended to a more complex reaction (OER). To evaluate the transferability of our descriptor framework, we systematically analyze angle–overpotential relationships across the same family of chalcogen-vacancy systems.

Initial screening of dopant-centered angles identifies $\angle S_1M_{74}S_6$ as the most promising candidate ($r = 0.85$, Fig. S8a–c). However, as observed with HER, extending our analysis to peripheral coordination shells substantially enhances correlation strengths. First-shell sulfur-centered angles, particularly the surface angle $\angle S_{15}S_{12}S_{19}$, exhibit a strong negative correlation with OER overpotential ($r = -0.90$, Fig. S9a–c), while second-shell sulfur-centered angles such as $\angle S_{11}S_{23}S_{22}$ demonstrate an equally significant positive correlation ($r = 0.90$, Fig. S10a–c), indicating that smaller angles in this descriptor family favor enhanced OER activity.

Extending our analysis to Mo-centered angles in the outer coordination shells reveals that the internal angle $\angle S_8Mo_{52}S_{36}$, centered on the outermost Mo_{52} atom, exhibits a good correlation ($r = 0.91$, Fig. 3a), slightly exceeding all S-centered descriptors. We therefore establish this Mo-centered angle as the optimal OER descriptor, designated φ_{OER} (Fig. 3b). This descriptor identifies $Pt_1@MoS_2$–S as the most promising catalyst within the $TM_1@MoS_2$–S system, with $\varphi_{OER} = 67.98°$ corresponding to a predicted overpotential of 0.51 V.

The robustness of φ_{OER} is confirmed through rigorous validation across four distinct material systems though we note that experimental OER validation is not performed in the present work: $TM_1@MoS_2$–S ($r = 0.91$), $TM_1@WSe_2$–Se ($r = 0.89$), $TM_1@WS_2$–S ($r = 0.85$), and $TM_1@MoSe_2$–Se ($r = 0.86$) (Fig. 3c–f). Among these, $Pt_1@WSe_2$–Se exhibits the highest predicted activity with $\varphi_{OER} = 68.92°$ corresponding to an overpotential of 0.36 V, while $Pt_1@WS_2$–S ($\varphi_{OER} = 68.21°$) and $Pt_1@MoSe_2$–Se ($\varphi_{OER} = 71.02°$) show predicted overpotentials of 0.56 V and 0.60 V, respectively.

Our results demonstrate that the angular descriptor framework successfully transfers from HER to OER, revealing both universal principles and reaction-specific characteristics. While both optimal descriptors, φ_{HER} ($\angle S_1S_{23}S_8$) for HER and φ_{OER} ($\angle S_8Mo_{52}S_{36}$) for OER, exhibit strong correlations with their respective activities ($r = 0.85$ and 0.91), confirming that coordination shell geometry governs catalytic performance across different electrochemical reactions, OER displays significantly greater angular sensitivity. This is evidenced by both higher maximum correlation coefficients and a greater number of angles exhibiting $|r| > 0.8$. We attribute this enhanced sensitivity to the more complex OER mechanism, which involves multiple adsorbed intermediates along a convoluted reaction pathway, making it particularly susceptible to subtle geometric variations. Crucially, despite these mechanistic differences, both reactions adhere to a unified design principle in which dopants modulate catalytic activity primarily through long-range structural perturbations in peripheral environments rather than through local metal-centered effects. This fundamental understanding establishes angular descriptors as a universal strategy for geometry-informed catalyst design across diverse electrochemical processes.

Transferability of angular descriptors from chalcogen-vacancy to metal-vacancy systems

After establishing the efficacy of angular descriptors in chalcogen-vacancy systems, we move on to investigate their applicability to the fundamentally distinct metal-vacancy configurations. MX_2 materials offer diverse doping sites,[48,49] with surface chalcogen vacancies and subsurface metal vacancies representing two predominant configurations that yield substantially different reactive sites and catalytic behaviors.[50,51] To assess the universal applicability of our descriptor framework, we extend our investigation to transition metal SACs formed by substituting Mo/W sites within the MX_2 lattice, which maintain the characteristic sandwich-like coordination geometry but position the active site differently (Fig. 4a for MoS_2 and Fig. 4d for WSe_2; atomic labeling in Fig. S7). In these metal-vacancy systems, reaction intermediates adsorb at surface chalcogen atoms rather than at the dopant site.

Our descriptor mining methodology proves equally effective in identifying key angular parameters within these metal-

vacancy systems. Through systematic coordination shell analysis, we visualize the correlation landscape using a color-coded scheme (Fig. 4b and e), where dark red ($r = -1$ to -0.5) and dark blue (r = 0.5 to 1) represent the strongest correlations. This analysis reveals two highly predictive angular descriptors: $\varphi_{HER\text{-}Mo}$ (an internal angle of $\angle S_7S_{19}Mo_{69}$ in MoS_2 systems, Fig. 4b) and $\varphi_{HER\text{-}W}$ (an internal angle of $\angle Se_{39}W_{56}W_{66}$ in WSe_2, Fig. 4e), collectively designated as $\varphi_{HER\text{-}M}$. These descriptors exhibit robust yet fundamentally distinct correlations with ΔG_{*H}. Specifically, $\varphi_{HER\text{-}Mo}$ displays a significant negative correlation ($r = -0.81$), where larger angles correspond to enhanced HER activity (Fig. 4c). Accordingly, $V_1@MoS_2$–Mo emerges as the most active catalyst in this series with $\varphi_{HER\text{-}Mo}$ = 139.31° and a near-optimal ΔG_{*H} = 0.01 eV, while the least active $Pt_1@MoS_2$–Mo shows $\varphi_{HER\text{-}Mo}$ = 139.41° with a strongly binding ΔG_{*H} of −1.65 eV. Conversely, $\varphi_{HER\text{-}W}$ demonstrates a strong positive correlation ($r = 0.86$), where increasing angular values improve catalytic performance (Fig. 4f). The optimal $Ir_1@WSe_2$–W displays $\varphi_{HER\text{-}W}$ = 47.06° with ΔG_{*H} = −0.08 eV, whereas $Mo_1@WSe_2$–W, which shows the lowest HER activity, exhibits $\varphi_{HER\text{-}W}$ = 47.70° with ΔG_{*H} = 1.26 eV.

The consistently high correlation strengths (average $|r| > 0.8$) across both vacancy types establish the universal predictive power and good transferability of angular descriptors in $TM_1@MX_2$ catalysts. However, we observe a fundamental distinction in descriptor behavior between the two systems: chalcogen-vacancy systems employ a universal descriptor (φ_{HER} = $\angle S_1S_{23}S_8$) across all catalysts, whereas in metal-vacancy systems, different atomic angles serve as the key descriptors, such as $\angle S_7S_{19}Mo_{69}$ and $\angle Se_{39}W_{56}W_{66}$. This divergence in correlation patterns stems from fundamental differences in how the two vacancy types perturb the electronic structure, a phenomenon we quantitatively explore in the following electronic structure investigation.

Electronic origins of angle–activity relationships

The established correlations between angular descriptors and catalytic activity prompt us to investigate their underlying electronic origins. While the connection between structural distortions and catalytic performance is known to be mediated by electronic structure,[52–54] conventional electronic descriptors show limited effectiveness in single-atom systems. Our systematic density of states (DOS) analysis of $TM_1@MoS_2$–S reveals the inadequacy of the conventional d-band center (ε_d) theory for SACs. As shown in Fig. S11 and S12, ε_d shows only weak correlations with both HER (ΔG_{*H}, $r = -0.30$) and OER (overpotential η, $r = 0.32$) activity. This limitation likely originates from fundamental characteristics of SACs: (i) anisotropic d-orbital/adsorbate interactions create orientation-dependent binding energies that are averaged out in ε_d analysis; (ii) the localized nature of catalytic activity in SACs depends on specific

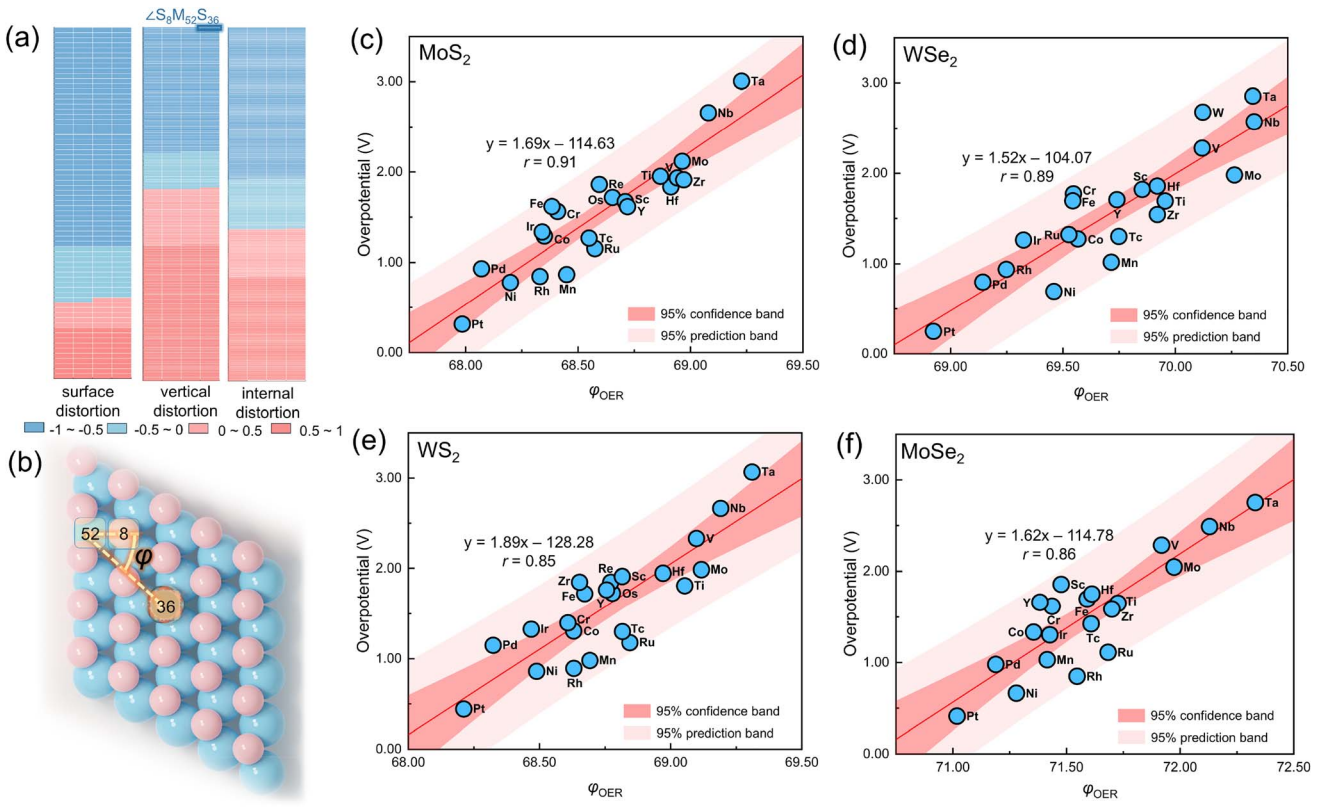

Fig. 3 Angular descriptors for OER activity in $TM_1@MX_2$–X systems. (a) Correlation matrix of angle–overpotential relationships, identifying the internal angle of $\angle S_8Mo_{52}S_{36}$ as exhibiting the strongest correlation. (b) Atomic configuration of the optimal descriptor $\angle S_8Mo_{52}S_{36}$ (denoted as φ_{OER}). (c–f) Linear regression analysis demonstrating the robust correlation between φ_{OER} and OER overpotential across different substrates: (c) MoS_2, (d) WSe_2, (e) WS_2, and (f) $MoSe_2$.

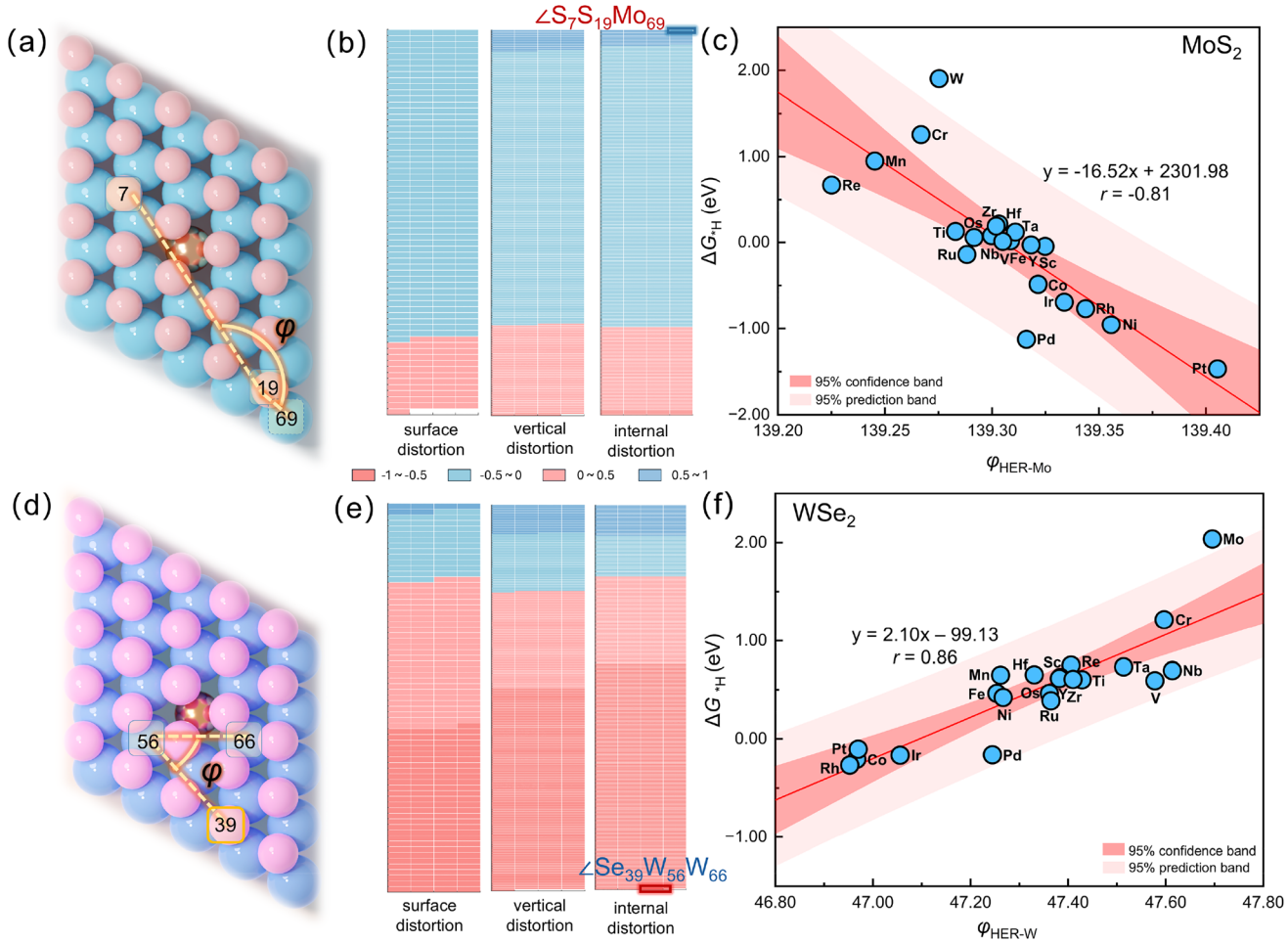

Fig. 4 Angular descriptors for HER activity in $TM_1@MX_2$ (metal-vacancy) systems. (a) Atomic configuration of the $TM_1@MoS_2$–Mo showing the optimal angular descriptor $\angle S_7S_{19}Mo_{69}$, with blue, pink, and gold spheres representing Mo, S, and dopant atoms, respectively. (b) Correlation matrix of angle–ΔG_{*H} correlation, identifying the internal angle of $\angle S_7S_{19}Mo_{69}$ exhibiting the strongest negative correlation. (c) Linear regression analysis of the correlation between $\angle S_7S_{19}Mo_{69}$ and ΔG_{*H}. (d) Atomic configuration of the $TM_1@WSe_2$–W featuring the optimal descriptor $\angle Se_{39}W_{56}W_{66}$, with purple, light red, and gold spheres representing W, Se, and dopant atoms, respectively. (e) Correlation matrix identifying the internal angle of $\angle Se_{39}W_{56}W_{66}$ as showing the strongest positive correlation. (f) Linear regression analysis of the correlation between $\angle Se_{39}W_{56}W_{66}$ and ΔG_{*H}.

orbital contributions rather than global d-band properties. These observations underscore the need for descriptors that can bridge atomic-scale geometry with electronic structure—not as a replacement for all existing descriptors, but as an additional perspective.

To address these limitations, we develop a multidimensional descriptor framework integrating d-band and p-band center theory with our angular descriptors (φ_{HER} and φ_{OER}).[55,56] Inspired by the binary descriptor approach,[32] we apply the SISSO algorithm[57] to derive band-structure descriptors $I_{band\text{-}HER}$ and $I_{band\text{-}OER}$. These incorporate s-, p-, and d-band contributions from both dopant TM_1 ($\varepsilon_{M\text{-}s}$, $\varepsilon_{M\text{-}d}$) and surrounding atoms ($\varepsilon_{23\text{-}p}$, $\varepsilon_{1\text{-}s}$, $\varepsilon_{36\text{-}p}$, $\varepsilon_{52\text{-}s}$).

The $I_{band\text{-}HER}$ descriptor shows an outstanding correlation with ΔG_{*H} ($r = 0.88$, Fig. 5a) and a strong anti-correlation with φ_{HER} ($r = -0.85$, Fig. 5b). These dual correlations reveal a coherent structure–activity relationship: while individual orbital bands provide incomplete activity descriptions, the integrated $I_{band\text{-}HER}$ descriptor captures essential electronic features governing HER performance, including band-center positions, bandwidth distributions, and multi-orbital coupling. More importantly, these results establish a fundamental mechanistic link: geometric distortions directly modulate the catalyst's electronic band structure, which in turn regulates ΔG_{*H} through coordinated s-, p-, and d-orbital interactions. This provides an atomic-level understanding of how structural modifications drive catalytic enhancements in $TM_1@MX_2$–X systems.

$$I_{band\text{-}HER} = \frac{\varepsilon_{M\text{-}s} + \varepsilon_{23\text{-}p}}{\varepsilon_{M\text{-}d} + \varepsilon_{1\text{-}s}}, \quad (1)$$

where $\varepsilon_{M\text{-}s}$ and $\varepsilon_{M\text{-}d}$ represent the s and d-band center values of the doped metal TM_1, respectively; $\varepsilon_{23\text{-}p}$ and $\varepsilon_{1\text{-}s}$ represent the p-band center value of atom S_{23} and the s-band center value of atom S_1 in angle $\angle S_1S_{23}S_8$, respectively (Tables S1–4).

Extending our descriptor framework to OER, the composite descriptor $I_{band\text{-}OER}$ integrates key electronic features: $\varepsilon_{M\text{-}s}$ and

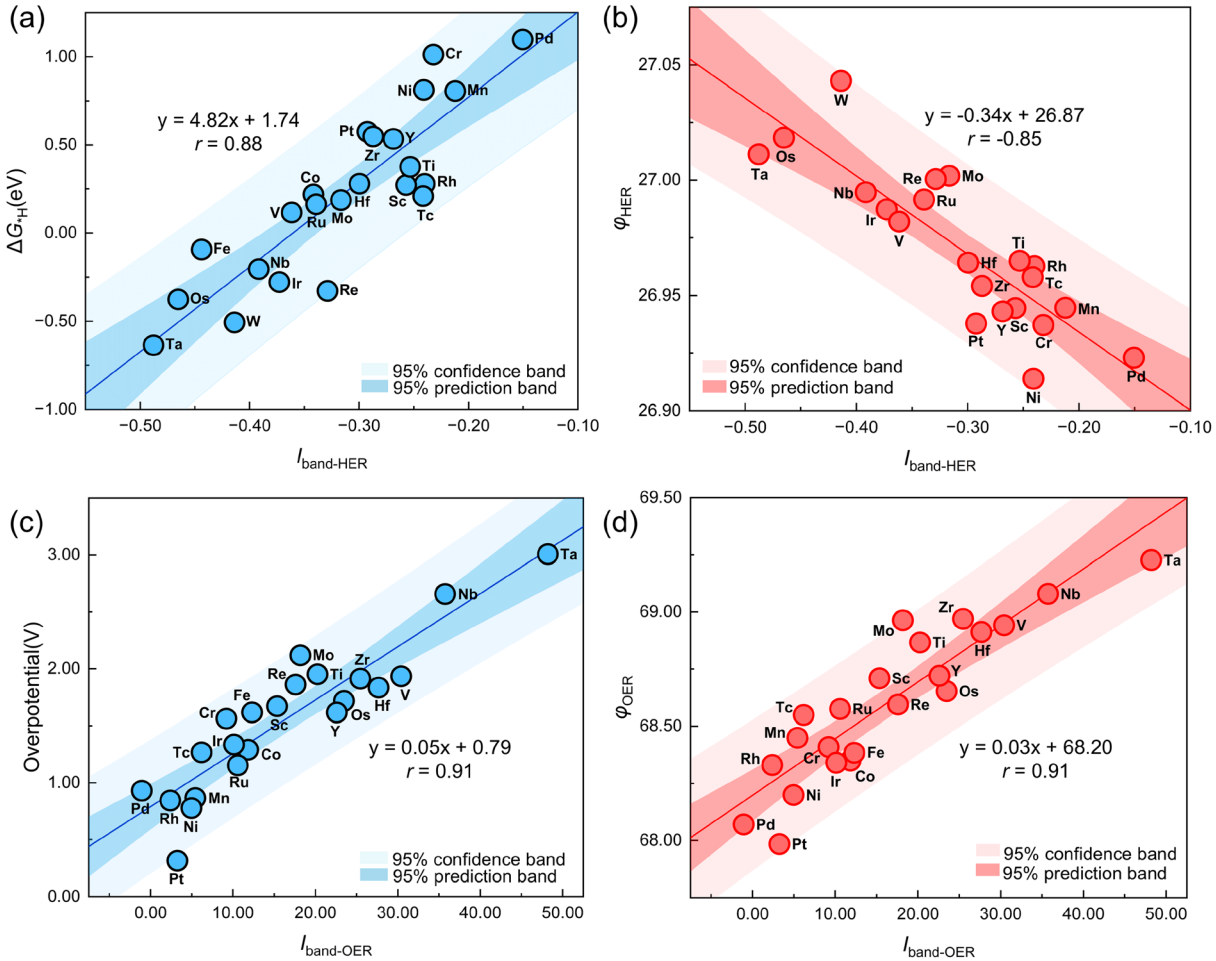

Fig. 5 Correlations between composite electronic descriptors and catalytic activities for TM_1@MoS_2–S. (a) Linear relationship between $I_{band\text{-}HER}$ and ΔG_{*H}. (b) Linear correlation between $I_{band\text{-}HER}$ and the optimal angular descriptor $\angle S_1S_{23}S_8$ (φ_{HER}). (c) Linear relationship between $I_{band\text{-}OER}$ and OER overpotential. (d) Linear correlation between $I_{band\text{-}OER}$ and the optimal angular descriptor $\angle S_8Mo_{52}S_{36}$ (φ_{OER}).

$\varepsilon_{M\text{-}d}$ represent the s- and d-band centers of the dopant TM_1, while $\varepsilon_{36\text{-}p}$ and $\varepsilon_{52\text{-}s}$ correspond to the p-band center of S_{36} and s-band center of Mo_{52} within the $\angle S_8Mo_{52}S_{36}$ angular configuration. Remarkably, $I_{band\text{-}OER}$ demonstrates good dual linear correlations with both φ_{OER} and OER overpotential, achieving identical correlation coefficients of $r = 0.91$ (Fig. 5c and d). These robust relationships establish that dopant-induced structural modifications systematically alter catalyst geometry, which linearly modulates OER activity through well-defined electronic structure changes.

$$I_{band\text{-}OER} = (\varepsilon_{M\text{-}d} - \varepsilon_{36\text{-}p}) \times \varepsilon_{M\text{-}s} \times \varepsilon_{52\text{-}s}, \quad (2)$$

The versatility of our electronic descriptor framework is further demonstrated by its successful application to metal-vacancy systems. For TM_1@MoS_2–Mo, $I_{band\text{-}Mo}$ incorporates $\varepsilon_{M\text{-}s}$ and $\varepsilon_{M\text{-}d}$ from the dopant TM_1, along with $\varepsilon_{19\text{-}p}$ and $\varepsilon_{69\text{-}s}$ (p-band center of S_{19} and s-band center of S_{69}) derived from the key angle $\angle S_7S_{19}Mo_{69}$ (Table S5). $I_{band\text{-}Mo}$ exhibits a significant correlation with ΔG_{*H} ($r = 0.71$, Fig. S13) and a strong anti-correlation with $\varphi_{HER\text{-}Mo}$ ($r = -0.67$, Fig. S14). Similarly, for TM_1@WS_2–W, $I_{band\text{-}W}$ integrates $\varepsilon_{M\text{-}p}$ (p-band center of TM_1) and $\varepsilon_{56\text{-}d}$ (d-band center of W_{56}) from $\angle Se_{39}W_{56}W_{66}$ (Table S6), demonstrating strong anti-correlations with both ΔG_{*H} ($r = -0.85$, Fig. S15) and $\varphi_{HER\text{-}W}$ ($r = -0.80$, Fig. S16).

$$I_{band\text{-}Mo} = \frac{\varepsilon_{19\text{-}p} - \varepsilon_{M\text{-}s}}{\varepsilon_{M\text{-}d} - \varepsilon_{69\text{-}s}}, \quad (3)$$

$$I_{band\text{-}W} = \left| e^{\varepsilon_{56\text{-}p}} - \frac{\varepsilon_{M\text{-}s}}{\Delta G_{*H}} \right|, \quad (4)$$

Our electronic structure analysis provides a unified mechanistic understanding of the observed descriptor behaviors across different vacancy types. Quantitative analysis reveals that metal doping induces markedly different electronic perturbations in the two systems: d-band center shifts of 0.008–0.640 eV in chalcogen-vacancy systems (Table S7), compared to substantially larger shifts of 0.013 to 1.760 eV in metal-vacancy systems (Table S8). This order-of-magnitude difference in electronic perturbation directly manifests in the geometric structure, explaining why angular descriptors exhibit limited transferability between vacancy types while maintaining strong

predictive power within each category. Importantly, these results successfully resolve the "structural distortion → electronic structure → catalytic activity" causal chain in $TM_1@MX_2$ catalysts through electronic descriptors that surpass conventional single-parameter approaches.

Reliability assessment

To rigorously evaluate the predictive accuracy of our angular descriptors, we perform systematic comparisons between descriptor-estimated catalytic activities and their corresponding DFT-computed values across all descriptor families: φ_{HER} (Fig. S17–20), φ_{OER} (Fig. S21–24), and $\varphi_{HER\text{-}M}$ (Fig. S25 and 26). The predictive performance is quantified by analyzing the slopes between predicted and computed values, where slopes approaching unity indicate superior accuracy. Our analysis demonstrates that all angular descriptors exhibit remarkable agreement with DFT benchmarks, confirming their reliability for catalytic activity prediction.

We further evaluate the practical utility of our framework by comparing descriptor-predicted activity trends with experimentally measured performances from published studies. Experimental overpotentials, compiled as averaged values from previous studies, are benchmarked against theoretical predictions obtained by converting ΔG_{*H} to overpotential *via* $\eta = |\Delta G_{*H}|/e$. As shown in Fig. 6a, theoretical predictions for $Co_1@MoS_2$–S,[34,58,59] $Pt_1@MoS_2$–S,[60–62] $V_1@MoS_2$–S,[63] and $Ir_1@MoS_2$–S align well with experimental trends. Notably, $Ir_1@MoS_2$–S is predicted to exhibit good HER activity with an overpotential of only 0.11 V. Correspondingly, as shown in Fig. S27, $Ru_1@MoS_2$–S,[64] $Co_1@MoS_2$–S,[65] and $Ni_1@MoS_2$–S[66]

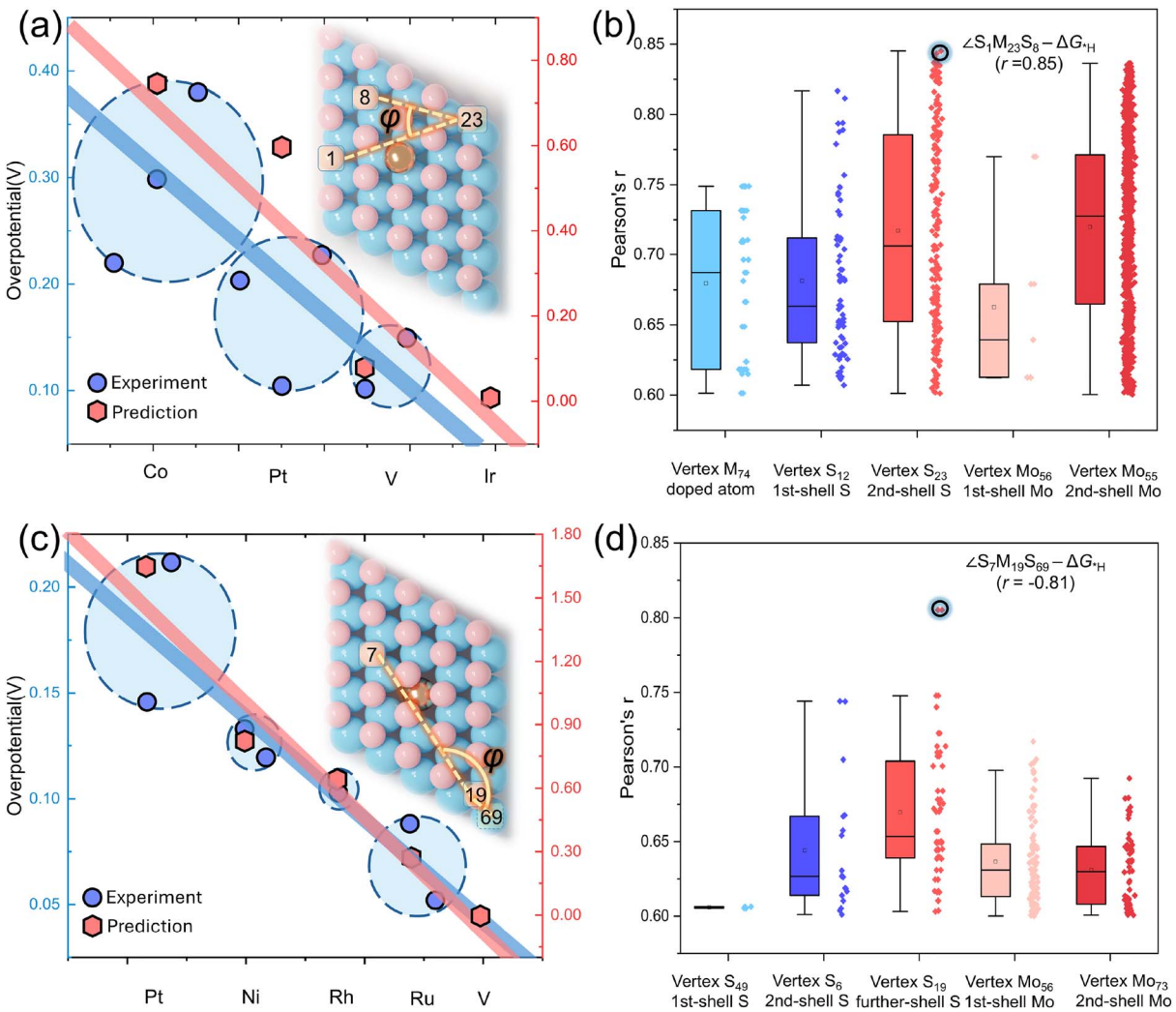

Fig. 6 Reliability assessment of angular descriptors. (a) Comparison between experimental measurements and φ_{HER}-predicted HER overpotential in chalcogen-vacancy systems. Blue and red lines represent fits to experimental and predicted values, respectively. (b) Correlation distributions for angles centered on different atomic sites (from left to right): dopant atom (M_{74}), first-shell sulfur (S_{12}), second-shell sulfur (S_{23}), first-shell molybdenum (Mo_{56}), and second-shell molybdenum (Mo_{55}). Box plots show statistical variations while overlaid curves indicate normal distributions. (c) Comparison between experimental measurements and $\varphi_{HER\text{-}Mo}$-predicted HER overpotential in metal-vacancy systems, with blue and red lines representing experimental and predicted fits, respectively. (d) Correlation distributions for angles centered on different atomic sites in metal-vacancy systems (from left to right): first-shell sulfur (S_{49}), second-shell sulfur (S_6), further-shell sulfur (S_{19}), first-shell molybdenum (Mo_{56}), and second-shell molybdenum (Mo_{73}).

show good agreement with the OER performance trends experimentally measured in the literature. Among them, $Pt_1@MoS_2$–S demonstrates optimal OER performance at 0.29 V, which aligns with experimental report of Pt SAC as efficient OER materials,[67] providing independent validation of our descriptor approach. These results validate the predictive capacity of our angular descriptors and establish a rational foundation for dopant selection in catalyst synthesis.

To investigate the spatial dependence of descriptor effectiveness, we systematically analyze angular descriptors centered on five representative atomic sites across coordination shells: the dopant M_{74}, first-shell S_{12}, second-shell S_{23}, first-shell Mo_{56}, and second-shell Mo_{55}. Considering only angles with meaningful correlations ($|r| > 0.6$, Fig. 6b), we observe that second-shell-centered angles are substantially more abundant than those from dopant or first-shell sites and exhibit higher average correlation coefficients. This spatial analysis definitively demonstrates that structural perturbations beyond the first coordination shell exert more substantial influence on HER activity than local metal-centered geometries.

The predictive power of angular descriptors is further validated in metal-vacancy systems through comparison of $\varphi_{\text{HER-Mo}}$-derived overpotentials with experimental values. The strong agreement between predictions and measurements for $Pt_1@MoS_2$–Mo,[35,68] $Ni_1@MoS_2$–Mo,[69,70] $Rh_1@MoS_2$–Mo,[71] and $Ru_1@MoS_2$–Mo[70,72] confirms descriptor transferability across vacancy types, with $V_1@MoS_2$–Mo exhibiting solid predicted HER activity (Fig. 6c). Supplementary analysis (Fig. 6d) filtering for angles with overpotential correlation $|r| > 0.6$ reveals that descriptors centered on outer-shell atoms are not only more numerous but also show stronger correlations, further highlighting the dominance of peripheral environments. While there is an optimal descriptor for HER, the results also indicate that some other angles exhibit good descriptive performance. The relatively reduced number of effective descriptors ($|r| > 0.6$) in Mo-vacancy systems compared to S-vacancy systems may originate from smaller atomic size mismatch between dopant and host metal atoms, resulting in less pronounced lattice distortions than those generated at chalcogen vacancy sites.

Experimental verification by case studies over $Ir_1@MoS_2$ and $V_1@MoS_2$

Guided by computational predictions identifying $Ir_1@MoS_2$ (S-vacancy) and $V_1@MoS_2$ (Mo-vacancy) as notable candidates, we synthesized these SACs with controlled atomic dispersion. X-ray diffraction (XRD) patterns (Fig. S28) confirm the phase purity of all samples. Notably, the characteristic diffraction peaks for $V_1@MoS_2$ and $Ir_1@MoS_2$ exhibit a slight but consistent shift toward lower angles compared to pristine MoS_2, which is indicative of lattice expansion induced by the doping of single-atom metal species into the MoS_2 matrix.[35,73] Aberration-corrected high-angle annular dark-field scanning transmission electron microscopy (AC HAADF-STEM) images provide direct visual evidence of single-atom dispersion state, which are consistent with Ir atoms occupying S-vacancy sites (Fig. 7a) and V atoms substituting the Mo sites (Fig. 7b). In addition, X-ray photoelectron spectroscopy (XPS) was performed to identify the electronic states. As shown in Fig. S29, the Ir $4f_{7/2}$ binding energy for $Ir_1@MoS_2$ is 62.70 eV, consistent with the oxidation state of Ir species. These configurations are consistent with our theoretically modelled $TM_1@MX_2$–X and $TM_1@MX_2$–M structures (Fig. 1b and c). The corresponding intensity line profiles (Fig. 7a and b insets) quantitatively corroborate the atomic-scale substitution, showing contrast variations consistent with the atomic numbers of the dopants (Ir, V) relative to the host atoms (S, Mo). We note that while AC HAADF-STEM provides direct visualization of single-atom dispersion and allows site assignment based on atomic number contrast, the precise local coordination remains inferred from microscopy contrast and image analysis.

The HER performance of $Ir_1@MoS_2$ was evaluated in an acidic electrolyte. Despite an ultralow loading of only 0.1 wt% Ir, this catalyst exhibits good activity, achieving a low overpotential of ~0.22 V at a current density of 10 mA cm^{-2} (Fig. 7c). With increasing content of Ir, the overpotential at 10 mA cm^{-2} decreases from 220 mV at 0.05% Ir to 216 mV at 0.1% Ir, then increases to 227 mV at a higher Ir content of 0.3% (Fig. S30). At the same time, the current densities at identical overpotentials present a volcanic trend with increasing Ir content. The optimum Ir content of 0.1% ($Ir_1@MoS_2$) leads to the highest HER activity. This performance is competitive with commercial Pt catalysts under identical conditions. To account for the minute precious metal content, we compared mass activities. As shown in Fig. 7d, the mass activity of $Ir_1@MoS_2$ at −0.05 V *vs.* RHE compares favorably with that of a commercial Pt/C catalyst with >20 wt% Pt loading. The electrochemically active surface area (ECSA), estimated *via* double-layer capacitance (C_{dl}) measurements (Fig. S31), increased from 16.4 mF cm^{-2} for pristine MoS_2 to 25.6 mF cm^{-2} for $Ir_1@MoS_2$, indicating a greater density of accessible active sites. Furthermore, $Ir_1@MoS_2$ demonstrates good stability, maintaining its activity through 1000 continuous cyclic voltammetry cycles (Fig. 7e). Moreover, electrochemical impedance spectroscopy (EIS) was employed to gain further insight into reaction kinetics and mechanisms. The charge transfer resistance (R_{ct}) was related to the electrocatalytic kinetics and its lower value corresponding to a faster reaction rate. Compared with MoS_2, $Ir_1@MoS_2$ possesses the lowest charge transfer resistance (Fig. S32). These results demonstrate that an ultralow content of Ir is essential to induce a high HER activity. The reaction step diagram shows that in $Ir_1@MoS_2$–S, the doped Ir_1 metal center site becomes the core active center for HER compared to other non-central surface sites (Fig. S33). Differential charge density and Bader charge analyses reveal that Ir_1 doping induces electron transfer from the surrounding Mo atoms to the Ir_1–H region, reconstructing the local electronic environment of MoS_2 and forming a strongly polarized adsorption site, thereby facilitating *H activation and enhancing HER performance (Fig. S34).

The earth-abundant $V_1@MoS_2$ catalyst also shows a substantial enhancement in HER activity compared to pristine MoS_2. Linear sweep voltammetry (LSV) in Ar-saturated 0.5 M H_2SO_4 shows that the overpotential required to achieve a current density of 10 mA cm^{-2} decreases significantly from

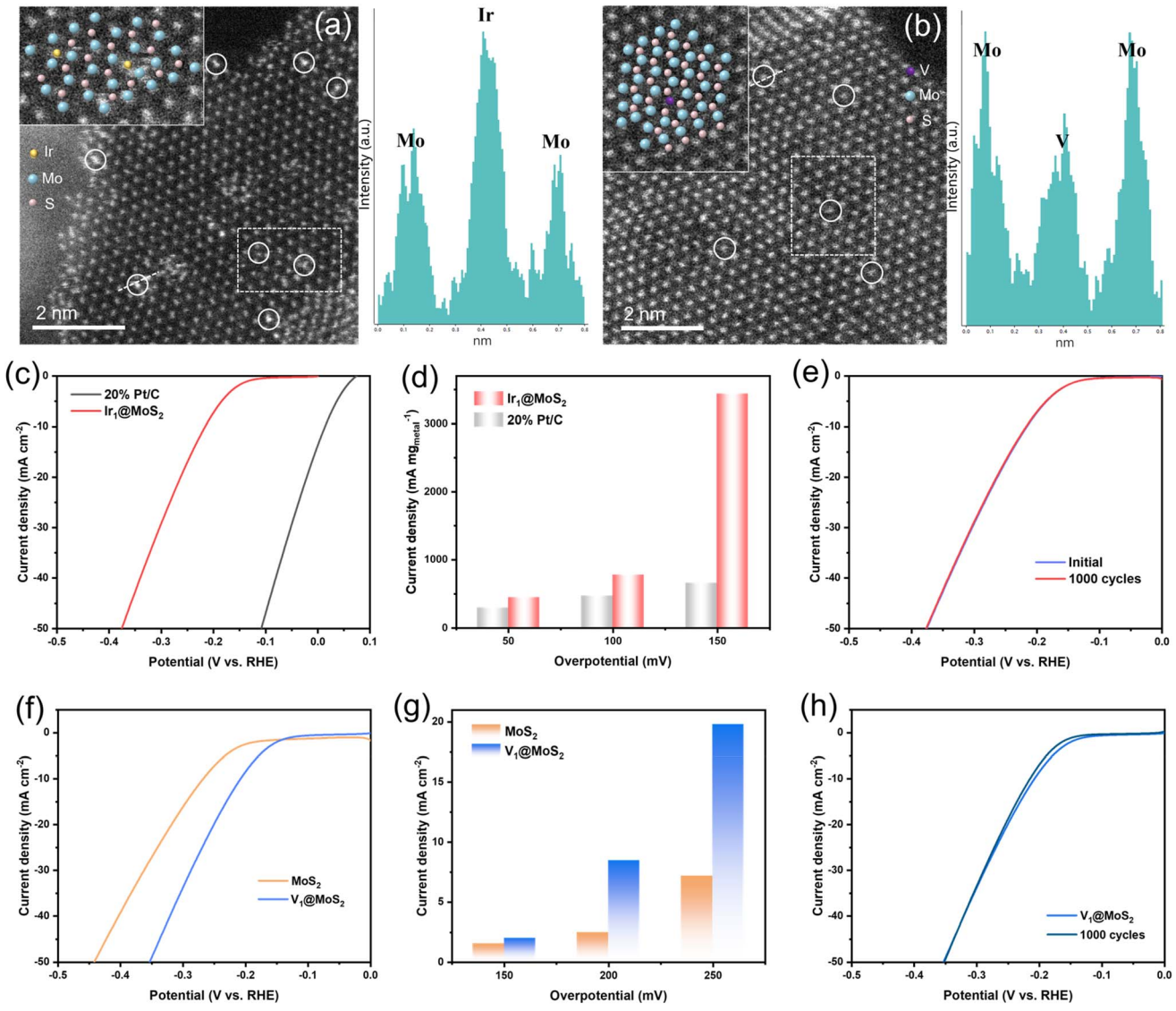

Fig. 7 Structural characterization and electrocatalytic HER performance of $Ir_1@MoS_2$ and $V_1@MoS_2$. (a) Aberration-corrected HAADF-STEM image of $Ir_1@MoS_2$, with the corresponding linear intensity profile demonstrating Ir single-atom substitution at S sites (inset: the atom distribution of Ir, Mo, and S in panel (a)). (b) Aberration-corrected HAADF-STEM image of the $V_1@MoS_2$, with the corresponding linear intensity profile demonstrating V single-atom substitution at Mo sites (inset: the atom distribution of V, Mo, and S in panel (b)). (c) HER polarization curves for the $Ir_1@MoS_2$ (0.1 wt% Ir) and commercial 20% Pt/C samples. (d) Comparison of current densities for $Ir_1@MoS_2$ and 20% Pt/C at different overpotentials. (e) Stability test of $Ir_1@MoS_2$ before and after 1000 CV cycles. (f) HER polarization curves for $V_1@MoS_2$ and pristine MoS_2. (g) Comparison of current densities for $V_1@MoS_2$ and pristine MoS_2 at different overpotentials. (h) Stability test of $V_1@MoS_2$ before and after 1000 CV cycles.

~0.27 V for pristine MoS_2 to ~0.22 V for $V_1@MoS_2$ (Fig. 7f). Across the tested potential range, $V_1@MoS_2$ consistently delivers current densities that are 2 to 3 times higher than those of the undoped baseline (Fig. 7g). This activity boost is supported by an increased C_{dl} value (Fig. S31), suggesting a more favorable surface structure or improved conductivity. $V_1@MoS_2$ also maintains good stability over 1000 CV cycles (Fig. 7h), demonstrating the inherent stability of the single-atom architecture within the MoS_2 lattice.

The exceptional experimental performance of both $Ir_1@MoS_2$ and $V_1@MoS_2$ provides strong validation for our computational framework. We compare the HER performance of $Ir_1@MoS_2$ and $V_1@MoS_2$ with currently reported excellent catalysts. Our catalysts exhibit good activity under ultra-low loading conditions, of which the intrinsic activity is superior to commercial Pt/C, demonstrating competitive performance under ultralow loading conditions.[58,62,74–77] These results emphasize that the key outcome is the descriptor-guided discovery, as our angular descriptors successfully led to experimentally active candidates and validated the predictive framework. Together, these case studies complete a rigorous design cycle, from data-driven descriptor discovery and theoretical screening to targeted synthesis and performance validation.

Discussion and conclusions

The rational design of advanced catalysts is fundamentally limited by a translational gap: we lack descriptors that are both predictive of activity and prescriptive for synthesis. While electronic-structure-based parameters have advanced our understanding, they often fail to translate into actionable geometric guidelines for experimentalists.[15–19] Critically, even promising structural descriptors, such as ensemble-averaged distortion metrics,[24] typically operate at a macroscopic level. They capture the existence of lattice strain or distortion, long recognized as crucial for catalysis, but lack the atomic-scale resolution to reveal which specific, local geometric motifs are functionally decisive. This gap between observing macroscopic strain and deciphering its atomically precise origins has hindered the development of a true "synthesis-to-function" blueprint.

Our work bridges this gap by introducing angular descriptors as the missing link between macroscopic lattice distortion and atomic-scale catalytic function. We propose that the doping-induced macroscopic strains, often probed by techniques like HAADF-STEM and XRD, are fundamentally manifested and quantifiable as precise changes in key structural angles within the coordination network. Through systematic data mining of single-atom doped transition metal dichalcogenides, we decode this relationship, developing interpretable angular parameters that directly quantify how atomic-scale geometry governs catalytic activity. We demonstrate that activity correlates more strongly with long-range angular parameters, such as the surface-oriented angle $\angle S_1S_{23}S_8$ (φ_{HER}) and the internal torsion angle $\angle S_8Mo_{52}S_{36}$ (φ_{OER}), than with local coordination environments. These structural descriptors exhibit both remarkable predictive accuracy ($|r| > 0.81$ for HER, $|r| > 0.85$ for OER) and good transferability, precisely because they capture the essential geometric signatures of functional strain.

A fundamental insight emerging from this decoding process is the dominant role of peripheral structural environments over first-shell coordination spheres. This finding challenges conventional design paradigms and provides a new geometric principle: catalytic activity is tuned not merely by the immediate neighbors of the active site, but by how the dopant atom reconfigures the entire local lattice. This geometric dominance is electronically rooted in multi-orbital interaction mechanisms, which are quantitatively captured by our developed multidimensional electronic descriptor (I_{band}). This descriptor demonstrates superior predictive power ($|r| = 0.88$ for HER; $|r| = 0.91$ for OER) compared to conventional d-band theory, while providing a mechanistic understanding of how geometric distortions modulate electronic states and adsorption energetics.

The practical utility of our framework is demonstrated through experimental validation. Guided by our angular descriptors, we identified and synthesized Ir_1@MoS_2 (S-vacancy), which achieves a low overpotential of 0.22 V at an ultralow loading of 0.1 wt%. When normalized by precious metal content, the intrinsic activity surpasses that of commercial Pt/C catalysts requiring >20 wt% Pt. Simultaneously, the earth-abundant V_1@MoS_2 (Mo-vacancy) exhibits significantly enhanced HER activity compared to pristine MoS_2. These successes are not isolated discoveries; they are direct validations of the predictive framework that connects synthesizable atomic-scale geometry (specific doping-induced angles) to targeted high performance.

In conclusion, this work establishes a generalizable geometric framework for single-atom catalysis, demonstrating that "peripheral geometric regulation" applies across different reactions and vacancy types. By decoding macroscopic lattice distortion into key angular descriptors, we bridge the long-standing gap between structural effects and atomic-scale catalytic function. Unlike previous electronic-model – confined studies, our angular signatures can serve as a generalizable blueprint and predictors that show good transferability for the discovery of high-performance single-atom electrocatalysts for sustainable hydrogen production. Nevertheless, its applicability to other catalyst classes (*e.g.*, alloy nanoparticles or metal surfaces) and to more complex reaction networks remains to be explored.

Author contributions

B. G.: data curation, methodology, writing original draft, writing – review & editing; Y. C.: data curation, methodology, writing original draft, writing – review & editing; Y. W.: data curation, methodology, writing original draft, writing – review & editing; F. W.: visualization; F. L.: visualization; L. C.: visualization; J. L.: conceptualization, funding acquisition, supervision, project administration, writing – review & editing; X. F.: supervision; S. L.: conceptualization, funding acquisition, supervision, project administration, writing – review& editing.

Conflicts of interest

The authors declare no conflict of interest.

Data availability

The data supporting this article have been included as part of the article and supplementary information (SI). Supplementary information: the detailed information for the theoretical calculations and additional experiments. See DOI: https://doi.org/10.1039/d6sc01740a.

Acknowledgements

The present work was supported by the National Natural Science Foundation of China (22461160253, 22373017, 22502083, 22508379 and 22378379), the National Natural Science Foundation of Fujian Province of China (2024I0004), the "Chuying Program" for the Top Young Talents of Fujian Province, the China Postdoctoral Science Foundation (2024M751372) and the Jiangsu Funding Program for Excellent Postdoctoral Talent (2024ZB761). Part of DFT computations were conducted at the Supercomputing Centre of Fujian.

References

1 L.-M. Cao and C.-T. He, *Chin. J. Struct. Chem.*, 2026, **45**, 100814.
2 W. Shi, T. Shen, C. Xing, K. Sun, Q. Yan, W. Niu, X. Yang, J. Li, C. Wei, R. Wang, S. Fu, Y. Yang, L. Xue, J. Chen, S. Cui, X. Hu, K. Xie, X. Xu, S. Duan, Y. Xu and B. Zhang, *Science*, 2025, **387**, 791–796.
3 H. Chen, L. Wang, M. Na and X. Zou, *Chem. Sci.*, 2025, **16**, 20662–20676.
4 H. Zeng, Z. Chen, Q. Jiang, Q. Zhong, Y. Ji, Y. Chen, J. Li, C. Liu, R. Zhang, J. Tang, X. Xiong, Z. Zhang, Z. Chen, Y. Dai, C. Li, Y. Chen, D. Zhao, X. Li, T. Zheng, X. Xu and C. Xia, *Nat. Commun.*, 2025, **16**, 4314.
5 Q. Deng, Z. Li, R. Huang, P. Li, H. Gomaa, S. Wu, C. An and N. Hu, *J. Mater. Chem. A*, 2023, **11**, 24434–24453.
6 L. Chang, Z. Sun and Y. H. Hu, *Electrochem. Energy Rev.*, 2021, **4**, 194–218.
7 Y. Liu, M. Han, Q. Xiong, S. Zhang, C. Zhao, W. Gong, G. Wang, H. Zhang and H. Zhao, *Adv. Energy Mater.*, 2019, **9**, 1803935.
8 M. Urso, X. Ju, R. Nittoor-Veedu, H. Lee, D. Zaoralová, M. Otyepka and M. Pumera, *ACS Catal.*, 2025, **15**, 11617–11663.
9 S. Yuan, Y. Zheng, Y. Chu, C. Xia, R. Dong, J. Xu, B. Teng, Y. Wu and Y. He, *Green Energy Environ.*, 2025, S246802572500189X.
10 J. Han, H. Wang, Y. Wang, H. Zhang, J. Li, Y. Xia, J. Zhou, Z. Wang, M. Luo, Y. Wang, N. Wang, E. Cortés, Z. Wang, A. Vomiero, Z. Huang, H. Ren, X. Yuan, S. Chen, D. Feng, X. Sun, Y. Liu and H. Liang, *Angew. Chem., Int. Ed.*, 2024, **63**, e202405839.
11 X. Li, J. Wang, H. Xue, L. Zhao, J. Lu, H. Zhang, M. Yan, F. Deng and C. Hu, *Adv. Funct. Mater.*, 2025, **35**, 2503360.
12 T. Sun, T. Yang, W. Zang, J. Li, X. Sheng, E. Liu, J. Li, X. Hai, H. Lin, C. H. Chuang, C. Su, M. Fan, M. Yang, M. Lin, S. Xi, R. Zou and J. Lu, *ACS Nano*, 2025, **19**, 5447–5459.
13 P. Cao, X. Mu, F. Chen, S. Wang, Y. Liao, H. Liu, Y. Du, Y. Li, Y. Peng, M. Gao, S. Liu, D. Wang and Z. Dai, *Chem. Soc. Rev.*, 2025, **54**, 3848–3905.
14 M. Li, J. Li, X. Zheng and Y. Zhou, *Rare Met.*, 2024, **43**, 4019–4037.
15 A. A. Latimer, A. R. Kulkarni, H. Aljama, J. H. Montoya, J. S. Yoo, C. Tsai, F. Abild-Pedersen, F. Studt and J. K. Nørskov, *Nat. Mater.*, 2017, **16**, 225–229.
16 F. Studt, F. Abild-Pedersen, T. Bligaard, R. Z. Sørensen, C. H. Christensen and J. K. Nørskov, *Science*, 2008, **320**, 1320–1322.
17 J. Noh, S. Back, J. Kim and Y. Jung, *Chem. Sci.*, 2018, **9**, 5152–5159.
18 G. Cao, S. Yang, J.-C. Ren and W. Liu, *Nat. Commun.*, 2025, **16**, 1251.
19 J. Li, M. Chen, P. Wang, X. Li, Y. Huang, K. Ding, L. Mao, X. Xiang and X. Chen, *Chem. Sci.*, 2025, **16**, 22071–22083.
20 X. Sun, R. B. Araujo, E. C. Dos Santos, Y. Sang, H. Liu and X. Yu, *Chem. Soc. Rev.*, 2024, **53**, 7392–7425.
21 H. Xu, J. Wang, J. Liu and D. Cheng, *Acc. Chem. Res.*, 2025, **58**, 2535–2549.
22 J. Wang, M. Zheng, X. Zhao and W. Fan, *ACS Catal.*, 2022, **12**, 5441–5454.
23 M. Li, Y. Cheng, C. Shao and Y. Li, *Chin. J. Chem. Phys.*, 2025, **38**, 199–211.
24 R. Chattot, O. L. Bacq, V. Beermann, S. Kühl, J. Herranz, S. Henning, L. Kühn, T. Asset, L. Guétaz, G. Renou, J. Drnec, P. Bordet, A. Pasturel, A. Eychmüller, T. J. Schmidt, P. Strasser, L. Dubau and F. Maillard, *Nat. Mater.*, 2018, **17**, 827–833.
25 R. B. Wexler, J. M. P. Martirez and A. M. Rappe, *J. Am. Chem. Soc.*, 2018, **140**, 4678–4683.
26 C. Ren, Y. Cui, Q. Li, C. Ling and J. Wang, *J. Am. Chem. Soc.*, 2025, **147**, 13610–13617.
27 H. Xu, D. Cheng, D. Cao and X. C. Zeng, *Nat. Catal.*, 2024, **7**, 207–218.
28 W. Shu, J. Li, J. X. Liu, C. Zhu, T. Wang, L. Feng, R. Ouyang and W. X. Li, *J. Am. Chem. Soc.*, 2024, **146**, 8737–8745.
29 F. Wei, L. Cao, B. Ge, Y. Chen, X. Pan, Y. Chai, R. Jing, X. Hu, X. Wang, J. Lin and S. Lin, *Angew. Chem., Int. Ed.*, 2025, **64**, e202416912.
30 B. Ge, F. Wei, Q. Wan, H. Zhang, P. Yuan and S. Lin, *Precis. Chem.*, 2023, **1**, 429–436.
31 Y. Chai, F. Wei, L. Cao, X. Wang, S. Lin, J. Lin and T. Zhang, *Coord. Chem. Rev.*, 2025, **536**, 216649.
32 Z. Han, R. Gao, T. Wang, S. Tao, Y. Jia, Z. Lao, M. Zhang, J. Zhou, C. Li, Z. Piao, X. Zhang and G. Zhou, *Nat. Catal.*, 2023, **6**, 1073–1086.
33 C. Tang, L. Chen, H. Li, L. Li, Y. Jiao, Y. Zheng, H. Xu, K. Davey and S. Z. Qiao, *J. Am. Chem. Soc.*, 2021, **143**, 7819–7827.
34 M. Pan, X. Zhang, C. Pan, J. Wang and B. Pan, *ACS Appl. Mater. Interfaces*, 2023, **15**, 19695–19704.
35 J. Xu, G. Shao, X. Tang, F. Lv, H. Xiang, C. Jing, S. Liu, S. Dai, Y. Li, J. Luo and Z. Zhou, *Nat. Commun.*, 2022, **13**, 2193.
36 S. Wang, X. Ning, Y. Cao, R. Chen, Z. Lu, J. Hu, J. Xie and A. Hao, *Inorg. Chem.*, 2023, **62**, 6428–6438.
37 G. Liu, L. Ding, Y. Meng, A. Ali, G. Zuo, X. Meng, K. Chang, O. L. Li and J. Ye, *Carbon Energy*, 2024, **6**, e521.
38 Z. Duan, H. Xia, H. Li, G. Shao, Y. Ren, X. Tang, Q. Liu, J. Hong, S. Dai, Y. Lin, K. Suenaga, Y. He and S. Liu, *Rare Met.*, 2025, **44**, 3130–3140.
39 Z. Jiang, W. Zhou, C. Hu, X. Luo, W. Zeng, X. Gong, Y. Yang, T. Yu, W. Lei and C. Yuan, *Adv. Mater.*, 2023, **35**, 2300505.
40 T. W. Clarkson and L. Magos, *Crit. Rev. Toxicol.*, 2006, **36**, 609–662.
41 L. Järup, *Br. Med. Bull.*, 2003, **68**, 167–182.
42 G. Kresse and J. Furthmüller, *Phys. Rev. B: Condens. Matter Mater. Phys.*, 1996, **54**, 11169–11186.
43 C. Guan, X. Yue and Q. Xiang, *Adv. Mater.*, 2025, **37**, 2501209.
44 B. Zhou, B. Bai, X. Zhu, J. Guo, Y. Wang, J. Chen, Y. Peng, W. Si, S. Ji and J. Li, *J. Colloid Interface Sci.*, 2024, **653**, 1177–1187.
45 X. B. Han, C. Q. Jing, H. Y. Zu and W. Zhang, *J. Am. Chem. Soc.*, 2022, **144**, 18595–18606.

46 Y. Liu, L. Xing, Y. Liu, D. Lian, M. Chen, W. Zhang, K. Wu, H. Zhu, Z. Sun, W. Chen, P. Wu, D. Wang and Y. Ji, *Appl. Catal., B*, 2024, **353**, 124088.
47 T. Zhang, Q. Ye, Y. Liu, Q. Liu, Z. Han, D. Wu, Z. Chen, Y. Li and H. J. Fan, *Nat. Commun.*, 2025, **16**, 3644.
48 Z. J. Duan, H. Xia, H. Z. Li, G. L. Shao, Y. Z. Ren, X. Tang, Q. N. Liu, J. H. Hong, S. Dai, Y. C. Lin, K. Suenaga, Y. M. He and S. Liu, *Rare Met.*, 2025, **44**, 3130–3140.
49 Q. Jiang, H. Xu, K. S. Hui, Y. Wei, L. Liu, Z. Ye, C. Zha, M. Zheng, J. Lu and K. N. Hui, *Adv. Mater.*, 2025, **37**, 2415986.
50 Z. Shi, X. Zhang, X. Lin, G. Liu, C. Ling, S. Xi, B. Chen, Y. Ge, C. Tan, Z. Lai, Z. Huang, X. Ruan, L. Zhai, L. Li, Z. Li, X. Wang, G.-H. Nam, J. Liu, Q. He, Z. Guan, J. Wang, C. S. Lee, A. R. J. Kucernak and H. Zhang, *Nature*, 2023, **621**, 300–305.
51 Y. Jia, Y. Zhang, H. Xu, J. Li, M. Gao and X. Yang, *ACS Catal.*, 2024, **14**, 4601–4637.
52 A. Gaur, J. Sharma, G. Kaur, S. Mhin and H. Han, *Adv. Funct. Mater.*, 2025, e16674.
53 C. Yin, F. Mo, X. Li, F. Li, W. Xue, Q. Wang, R. Shi, Y. Zhao, A. Zeb, J. Wang, W. Liu, S. Zhan and Q. Zhou, *Appl. Catal., B*, 2025, **376**, 125470.
54 R. Wang, L. Zhang, J. Shan, Y. Yang, J. Lee, T. Chen, J. Mao, Y. Zhao, L. Yang, Z. Hu and T. Ling, *Adv. Sci.*, 2022, **9**, 2203917.
55 J. Wang, X. Li, B. Wei, R. Sun, W. Yu, H. Y. Hoh, H. Xu, J. Li, X. Ge, Z. Chen, C. Su and Z. Wang, *Adv. Funct. Mater.*, 2020, **30**, 1908708.
56 Y. Wang, D. Wang, J. Gao, X. Hao, Z. Li, J. Zhou and F. Gao, *Phys. Chem. Chem. Phys.*, 2020, **22**, 14537–14543.
57 R. Ouyang, S. Curtarolo, E. Ahmetcik, M. Scheffler and L. M. Ghiringhelli, *Phys. Rev. Mater.*, 2018, **2**, 083802.
58 T. H. M. Lau, X. Lu, J. Kulhavý, S. Wu, L. Lu, T. S. Wu, R. Kato, J. S. Foord, Y. L. Soo, K. Suenaga and S. C. E. Tsang, *Chem. Sci.*, 2018, **9**, 4769–4776.
59 S. Park, J. Park, H. Abroshan, L. Zhang, J. K. Kim, J. Zhang, J. Guo, S. Siahrostami and X. Zheng, *ACS Energy Lett.*, 2018, **3**, 2685–2693.
60 W. Yan, Z. Zhao, Z. Xin, J. Hu, J. Xia, L. Zhou, Y. Xu, Y. Zhang, K. Liu, R. Wang and Y. Sun, *Adv. Funct. Mater.*, 2025, **35**, 2423262.
61 M. Li, J. Xu, D. Liu, J. Yang, J. Lin, X. Xiao, Z. Wang, X. Liu, L. Jia, Y. Liu, C. Yao, Y. Li, Z. Lian and W. Yang, *Appl. Surf. Sci.*, 2024, **667**, 160384.
62 T. H. M. Lau, S. Wu, R. Kato, T. S. Wu, J. Kulhavý, J. Mo, J. Zheng, J. S. Foord, Y. L. Soo, K. Suenaga, M. T. Darby and S. C. E. Tsang, *ACS Catal.*, 2019, **9**, 7527–7534.
63 S. Bolar, S. Shit, N. C. Murmu, P. Samanta and T. Kuila, *ACS Appl. Mater. Interfaces*, 2021, **13**, 765–780.
64 V. H. Hoa, D. T. Tran, S. Prabhakaran, D. H. Kim, N. Hameed, H. Wang, N. H. Kim and J. H. Lee, *Nano Energy*, 2021, **88**, 106277.
65 X. Gong, Z. Jiang, W. Zeng, C. Hu, X. Luo, W. Lei and C. Yuan, *Nano Lett.*, 2022, **22**, 9411–9417.
66 G. Wang, G. Zhang, X. Ke, X. Chen, X. Chen, Y. Wang, G. Huang, J. Dong, S. Chu and M. Sui, *Small*, 2022, **18**, 2107238.
67 X. Xu, H. Xu and D. Cheng, *Nanoscale*, 2019, **11**, 20228–20237.
68 J. Deng, H. Li, J. Xiao, Y. Tu, D. Deng, H. Yang, H. Tian, J. Li, P. Ren and X. Bao, *Energy Environ. Sci.*, 2015, **8**, 1594–1601.
69 J. Ge, Y. Chen, Y. Zhao, Y. Wang, F. Zhang and X. Lei, *ACS Appl. Mater. Interfaces*, 2022, **14**, 26846–26857.
70 J. Ge, D. Zhang, Y. Qin, T. Dou, M. Jiang, F. Zhang and X. Lei, *Appl. Catal., B*, 2021, **298**, 120557.
71 X. Meng, C. Ma, L. Jiang, R. Si, X. Meng, Y. Tu, L. Yu, X. Bao and D. Deng, *Angew. Chem., Int. Ed.*, 2020, **132**, 10588–10593.
72 J. Wang, W. Fang, Y. Hu, Y. Zhang, J. Dang, Y. Wu, B. Chen, H. Zhao and Z. Li, *Appl. Catal., B*, 2021, **298**, 120490.
73 J. Zhu, Z. Wang, H. Yu, N. Li, J. Zhang, J. Meng, M. Liao, J. Zhao, X. Lu, L. Du, R. Yang, D. Shi, Y. Jiang and G. Zhang, *J. Am. Chem. Soc.*, 2022, **139**, 10216–10219.
74 Y. Qu, B. Chen, Z. Li, X. Duan, L. Wang, Y. Lin, T. Yuan, F. Zhou, Y. Hu, Z. Yang, C. Zhao, J. Wang, C. Zhao, Y. Hu, G. Wu, Q. Zhang, Q. Xu, B. Liu, P. Gao, R. You, W. Huang, L. Zheng, L. Gu, Y. Wu and Y. Li, *J. Am. Chem. Soc.*, 2019, **141**, 4505–4509.
75 R. Zhang, Y. Li, X. Zhou, A. Yu, Q. Huang, T. Xu, L. Zhu, P. Peng, S. Song, L. Echegoyen and F.-F. Li, *Nat. Commun.*, 2023, **14**, 2460.
76 H. Jiang, W. Yang, M. Xu, E. Wang, Y. Wei, W. Liu, X. Gu, L. Liu, Q. Chen, P. Zhai, X. Zou, P. M. Ajayan, W. Zhou and Y. Gong, *Nat. Commun.*, 2022, **13**, 6863.
77 Y. Shi, W.-M. Huang, J. Li, Y. Zhou, Z.-Q. Li, Y.-C. Yin and X.-H. Xia, *Nat. Commun.*, 2020, **11**, 4558.